BIOMIMETICS

Biomorphic structural batteries for robotics

Mingqiang Wang[1,2,3,4,5], Drew Vecchio[2,5], Chunyan Wang[1], Ahmet Emre[2,3,4,5], Xiongye Xiao[6], Zaixing Jiang[1], Paul Bogdan[6], Yudong Huang[1]*, Nicholas A. Kotov[2,3,4,5,7]*

Batteries with conformal shape and multiple functionalities could provide new degrees of freedom in the design of robotic devices. For example, the ability to provide both load bearing and energy storage can increase the payload and extend the operational range for robots. However, realizing these kinds of structural power devices requires the development of materials with suitable mechanical and ion transport properties. Here, we report biomimetic aramid nanofibers–based composites with cartilage-like nanoscale morphology that display an unusual combination of mechanical and ion transport properties. Ion-conducting membranes from these aramid nanofiber composites enable pliable zinc-air batteries with cyclic performance exceeding 100 hours that can also serve as protective covers in various robots including soft and flexible miniaturized robots. The unique properties of the aramid ion conductors are attributed to the percolating network architecture of nanofibers with high connectivity and strong nanoscale filaments designed using a graph theory of composite architecture when the continuous aramid filaments are denoted as edges and intersections are denoted as nodes. The total capacity of these body-integrated structural batteries is 72 times greater compared with a stand-alone Li-ion battery with the same volume. These materials and their graph theory description enable a new generation of robotic devices, body prosthetics, and flexible and soft robotics with nature-inspired distributed energy storage.

INTRODUCTION

Biomorphic macroscale devices have combinations of shape and functionalities similar to those found in living organisms similar in scale. Robotic devices are often inspired by biomorphism but not with respect to energy storage solutions. Conformal body-integrated energy storage is common in biology, represented by adipose tissues, which have several additional functionalities such as mechanical, thermal, and biochemical (*1*). Replacing traditional stand-alone batteries in robotic devices with conformal multifunctional biomorphic cells can enhance ground robotics, drones, and prosthetic devices through the simultaneous extension of their operational time and reduction in total weight.

Devices that combine energy storage and load-bearing functions are known as structural batteries. These batteries have been explored as a means to extend the operating time of electric vehicles (*2*–*5*) and drones (*6*). The stand-alone battery, however, held most of the energy required for these vehicles in all prior implementations of the concept, including an early implementation in a robotic device (*6*). Macroscale biological systems, of course, do not have battery-like organs. The transition to "battery-less" structural power in robotics would require a substantial increase in energy density. The engineering realization of a biomorphic structural battery as the sole source of power in a robotic device is impeded by available materials, which lack sufficient mechanical, chemical, and transport properties and methods for their structural design. In theory, these materials may have a variety of structural designs, but the difficult property requirements imposed on them may inevitably lead to nanoscale architectures mirroring some biological solutions to the same property conundrums. These biomimetic materials are typically based on artificial nanoscale components because their general ability to self-assemble unites biological and abiological matter with nanoscale dimensions.

Compared with rechargeable zinc ion batteries with MnO_2 cathode used previously in distributed energy storage in drones (*6*), zinc-air batteries are particularly attractive for use as biomorphic structural batteries because of their high theoretical energy density, which exceeds that of lithium-ion batteries by five times (*7*, *8*). Moreover, sufficient stiffness and pliability of zinc electrodes enable these batteries to be used as conformal load-bearing components. They are also environmentally friendly because both the cathode and anode are transition metal–free (*6*–*8*). However, Zn-air battery cells with dual functionalities are particularly difficult to implement as biomorphic batteries because of the lack of suitable ion-conducting membranes with high strength, stiffness, toughness, and ion transference numbers. Current versions of zinc-air cells have large inter-electrode gaps filled with liquid electrolytes that markedly limit their suitability for load-bearing components in any type of robot. Besides reductions in energy density, the highly caustic liquid electrolyte is prone to leaks, especially under strain (*7*–*9*). An alternative is to use gel or solid-state ion-conducting membranes; however, these devices often suffer from severe performance fade (*7*, *8*). Furthermore, the swelling-contraction cycle characteristic of hydroxide electrolytes (*8*, *10*, *11*) leads to delamination of the electrolyte membrane from electrodes, which prevents the realization of complex biomorphic shapes using zinc-air dual functionalities. Dendrite growth represents another serious materials-related problem, with stiff zinc dendrites that easily pierce the soft gel electrolyte layer (*12*). Solid electrolytes capable of transporting hydroxide ions suitable for zinc-air chemistry while having required toughness, stiffness, and strength will lead to new high-capacity structural batteries that are light, safe, and shape-adaptable, enabling a wide variety of implementations in

[1]School of Chemistry and Chemical Engineering, MIIT Key Laboratory of Critical Materials Technology for New Energy Conversion and Storage, State Key Laboratory of Urban Water Resource and Environment, Harbin Institute of Technology, Harbin 150001, P. R. China. [2]Department of Chemical Engineering, University of Michigan, Ann Arbor, MI 48109, USA. [3]Department of Biomedical Engineering, University of Michigan, Ann Arbor, MI 48109, USA. [4]Department of Materials Science and Engineering, University of Michigan, Ann Arbor, MI 48109, USA. [5]Biointerfaces Institute, University of Michigan, Ann Arbor, MI 48109, USA. [6]Ming Hsieh Department of Electrical and Computer Engineering, University of Southern California, Los Angeles, CA 90089, USA. [7]Michigan Institute of Transnational Nanotechnology (MITRAN), Ypsilanti, MI, USA.
*Corresponding author. Email: huangyd@hit.edu.cn (Y.H.); kotov@umich.edu (N.A.K.)

robotics. Biomimetic composites based on stiff nanofibers that self-assemble into a high-porosity open network could address these challenges because of their ability to redistribute strains over large volumes.

Here, we engineered a solid ion conductor for zinc-air batteries by taking advantage of the mechanical properties of aramid nanofibers (ANFs). To facilitate ion transport, the ANFs were combined with a soft ion-transporting component: quaternary ammonium functionalized polyvinyl alcohol (QUPA) (figs. S1 to S3). The mechanical and ion transport properties of our biomimetic QUPA/ANF composites can be rationalized by applying a graph theory (GT) description of the ANF network architecture. We attribute the performance of our composite to the percolating network architecture of ANF with high connectivity and strong nanoscale filaments. The high strength, stiffness, toughness, and ionic conductivity of these composites enables the realization of robots that do not need a stand-alone battery and have 72 times greater capacity compared to a Li-ion battery with the same volume.

RESULTS

Dispersions of branched ANFs with an average diameter of 30 to 40 nm and several microns in length were synthesized in dimethyl sulfoxide (DMSO) (*13*) starting with different amounts of the parent Kevlar 69 microfibers (see Materials and Methods and fig. S6C). ANF dispersions with concentrations of 0.5, 1.0, 1.5, and 2.0% [weight % (wt %)] were spin-coated onto solid substrates (*13*, *14*) and dried with supercritical CO_2; the resulting materials will be referred to here as ANF-0.5, ANF-1.0, ANF-1.5, and ANF-2.0. The morphologies of ANF-0.5, ANF-1.0, ANF-1.5, and ANF-2.0 can be characterized as percolating networks of nanofibers (Fig. 1, A to D). ANF-based (*6*) and other nanofibrous composites used in batteries (*15*, *16*) are biomimetic because their nanoscale structure is inspired by cartilage (*17*) and similar tissues, such as kidney membranes. Engineering of these biological tissues solves the same problem as ion-conducting membranes in batteries—the coupled optimization of ion transport and mechanical properties.

Unlike any prior studies on biomimetic or other composites, the fibrous architecture of the produced materials can be analyzed quantitatively via GT. In this formalism, the continuous ANF filaments are denoted as edges (aka links), whereas their intersections are denoted as nodes (aka vertices). The structure of the ANF network was processed using the software StructuralGT, which was developed in-house (see Materials and Methods). We found that GT indexes describing the network connectivity—such as graph density (GD), global efficiency (GE), average betweenness centrality (ABC), and average closeness centrality (ACC)—are nearly the same for ANF-0. 5, ANF-1.0, ANF-1.5, and ANF-2.0 (Fig. 1 and Table 1). These GT indexes describe different aspects of the network connectivity, and their constancy provides proof that the architecture of these percolating networks remains the same despite different preparatory conditions. Because scanning electron microscope (SEM) images display distinct self-similar connectivity patterns, this conclusion can also be tested by the multifractal analysis (MFA) of resulting graphs (Fig. 1E). As we learned before (*18*), the wideness of the multifractal spectrum $f(\alpha)$ in terms of Lipschitz-Holder exponents, α, quantifies the structural complexity and heterogeneity of a network. Here, α reflects the dimension of the fractal structure, and $f(\alpha)$ reflects the proportion of the fractal structure with Lipschitz-Holder exponent α, so the multifractal spectrum shows the distribution of fractal structures in the network. Alternatively stated, a delta function–like spectrum corresponds to a monofractal graph where a single physical rule governs the graph topology at any scale. In contrast, the wideness of the multifractal spectrum indicates that more than one physical rule contributes to the observed topology. Consequently, the similarities of the multifractal spectra for all of the GT representations of ANF networks indicate that all of the ANF-based percolating networks described here have multifractal characteristics and follow the same structural laws. The origin of the minimal variability in GD, GE, ABC, and ACC for ANF-0.5, ANF-1.0, ANF-1.5, and ANF-2.0 likely stems from the similarity of the building blocks of these networks.

To prepare ion-conducting membranes, the porous sheets of percolating ANF networks were impregnated with QUPA (Fig. 1, A to D), enabling the effective transport of hydroxide ions rather than metal ions used in other batteries with zinc anodes. Successful incorporation of the polyelectrolyte can be confirmed by thermogravimetric analysis (fig. S7), a considerable increase of thickness (Fig. 2, F to K, and figs. S8 to S9), and a large decrease of Brunauer-Emmett-Teller (BET) porosity from 214.4 to 13.2 $m^2 g^{-1}$ (fig. S10). The resulting composites will be referred to as QUPA/ANF-0.5, QUPA/ANF-1.0, QUPA/ANF-1.5, and QUPA/ANF-2.0, respectively. The mechanical properties of QUPA/ANF biomimetic composites showed gradual increase of all essential mechanical properties with increased concentrations of ANF dispersion (Fig. 1, F and G, and fig. S11). Concomitant improvement of tensile strength, Young's modulus, and toughness is notable because an increase in one typically coincides with a decrease in others. We attribute this property to the constancy of the materials architecture in parallel with the increase of the overall volumetric density of ANF and average diameter of nanoscale filaments. Specifically, the average diameters of the aramid filaments in ANF-0.5, ANF-1.0, ANF-1.5, and ANF-2.0 networks gradually increase to 28 ± 5, 34 ± 7, 38 ± 6, and 45 ± 8 nm, respectively. Given the fact that the material's architecture remains the same (Table 1 and Fig. 1E), the increase of the filament diameter is directly related to the improvement of the mechanical properties.

Because all of our composites showed little difference with respect to ion conductivity (fig. S12), the QUPA/ANF-2.0 material with the best mechanical properties observed among the spectrum of QUPA/ANF composites was chosen for implementation in biomorphic structural batteries. X-ray diffraction pattern (XRD) (Fig. 2C) and SEM images (figs. S4 and S5) of QUPA suggest that chemical modification with quaternary ammonium groups reduces crystallinity as indicated by the reduction of the XRD peak at 19.76° (*19*), which facilitates ionic conductivity (*20*–*22*). Comparing our ion-conducting materials with others highlights their unique combination of mechanical and charge transport properties. The tensile strength and Young's modulus were 20 ± 1.0 and 120 ± 6 MPa, respectively (Fig. 1, E to G, and tables S2 and S3) (*23*, *24*). Although improvements in Young's modulus are essential for defeating dendrite growth, fracture toughness and tensile toughness are particularly important for biomorphic structural batteries, and QUPA/ANF-2.0 displayed record values of 720 ± 60 J m^{-3} (fig. S15) and 3500 ± 180 J m^{-3} (fig. S11), respectively, which exceeds those of other OH^- conductors by 100 to 500% (*7*, *25*, *26*). Consequently, QUPA/ANF-2.0 membranes also display the ability to withstand large bending and other deformations (Fig. 2, D and E, and figs. S13 and S14) much better than other solid electrolytes. For example, the angular range in bending is hardly

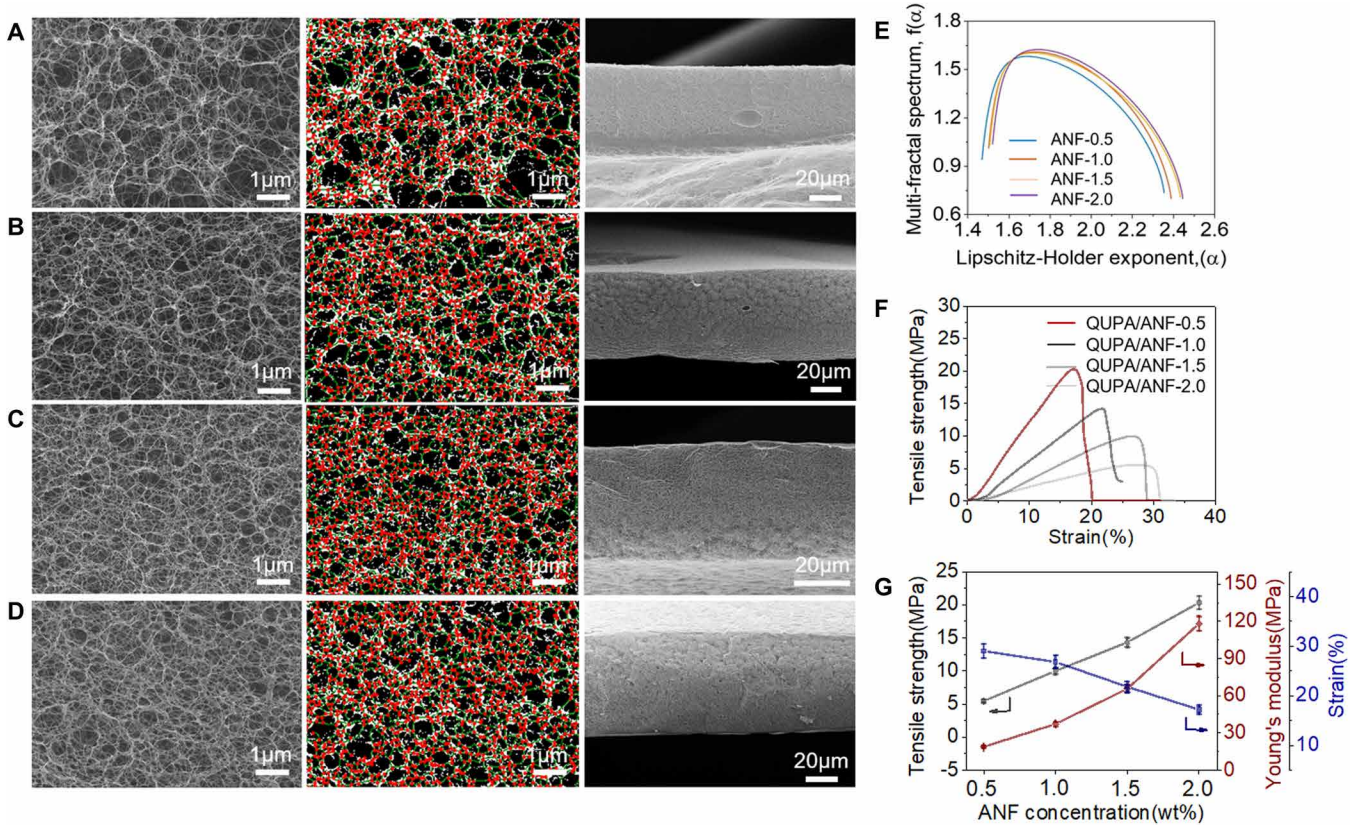

Fig. 1. Graph theoretical description of nanofiber composites and their mechanical properties. The left, middle, and right columns display SEM images of ANF composite surface, its GT representation obtained from StructuralGT, and SEM image of the membrane cross section, respectively. ANF aerogel membrane was prepared with different concentrations of ANF dispersion (**A**) 0.5, (**B**) 1.0, (**C**) 1.5, and (**D**) 2.0 wt %. (**E**) MFA of the GT representation for the ANF framework composites made for different ANF concentrations from 0.5 to 2.0 wt %. Typical stress-strain curves (**F**), tensile strength values, Young's modulus, and elongation at break (**G**) of QUPA/ANF with different ANF dispersion concentrations from 0.5 to 2.0 wt %. Young's modulus of the QUPA/ANF-2.0 is 85 times higher than that of QUPA ($E = 1.4 \pm 0.004$ MPa; table S2), which is much higher than those of fiber-enhanced polymer hydrogel (table S3).

Table 1. Graph theoretical enumerators for percolating nanoscale networks from ANFs.

Parameter	0.5 wt %	1.0 wt %	1.5 wt %	2.0 wt %
Graph density (GD)	0.012	0.011	0.010	0.013
Global efficiency (GE)	0.129	0.124	0.121	0.134
Avg. betweenness centrality (ABC)	0.040	0.038	0.034	0.039
Avg. closeness centrality (ACC)	0.080	0.070	0.070	0.078

accessible for other materials currently being evaluated as advanced battery electrolytes (*27*, *28*).

Furthermore, the ionic conductivity of QUPA/ANF-2.0 is 61.3 ± 3.1 mS cm^{-1}, which is 450% higher than that of polyvinyl alcohol (PVA) (13.6 ± 0.6 mS cm^{-1}) and 31.0% higher than that of QUPA (46.8 ± 2.4 mS cm^{-1}; Fig. 3A and fig. S16), indicating synergystic enhancement of both properties, which should be noted as a common effect in many biomimetic nanomaterials because of strong contribution of interfaces (*29*) and utilization of artificial nanoscale components (*30*). Despite the composite's solid state, the ionic conductivity of these composites is comparable or higher than that of ion-conducting gels from highly charged polycations (*31*, *32*), modified cellulose (*33*), and cellulose/graphene oxide composites (*34*). The electrochemical performance of QUPA/ANF-2.0 is also higher than that of the prototypical A201 membrane with ionic conductivity of 40 mS cm^{-1} (*31*, *33*) and comparable or better than solid-state ion-conducting membranes used in other zinc-air batteries (table S4). At higher temperatures, hydroxide ion conductivity is increased (fig. S17), as expected. Note that the activation energy for ion transport for QUPA/ANF-2.0 (E_a = 8.87 kJ mol^{-1}) is lower than that of QUPA

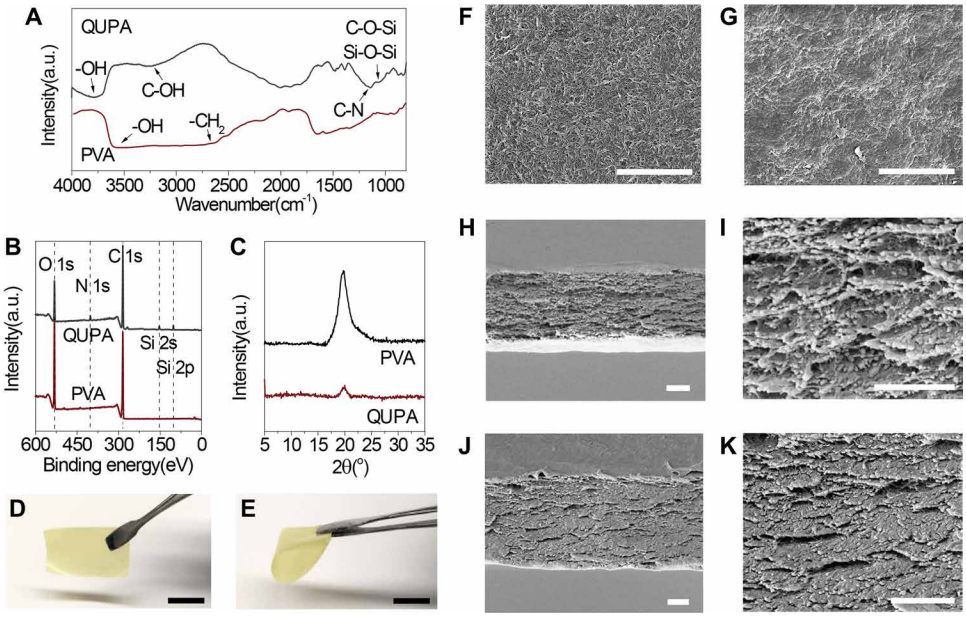

Fig. 2. Structural characterization of ion-conductive membranes. (**A** to **C**) PVA and functionalized QUPA composite comparison by FTIR spectra (A), wide XPS region spectrum (B), and XRD pattern (C). a.u., arbitrary units. (**D** and **E**) Photographs of QUPA/ANF-2.0 composite membrane in different states. (**F** and **G**) The comparison of surface SEM image of ANF-2.0 (F) and QUPA/ANF-2.0 (G). (**H**) The cross-section SEM images of the ANF-2.0 membrane prepared by the spin-coating method and its magnified image (**I**). (**J** and **K**) SEM images of QUPA/ANF-2.0 after soaking in polymer solution. Scale bars, (D and E) 1 cm and (F and K) 2.0 μm.

(E_a = 11.7. kJ mol^{-1}) and PVA (E_a = 25.7 kJ mol^{-1}) (fig. S18 and table S5), which is indicative of a functional synergy between percolating network of ANF and QUPA.

In addition to high ionic conductivity, QUPA/ANF-2.0 exhibits enhanced ion exchange capacity (IEC) of 2.96 mmol g^{-1} and a high ion concentration of 1.15 mmol cm^{-3}, which are much higher than those of QUPA (2.08 mmol g^{-1}, 0.76 mmol cm^{-3}) and PVA gel membranes (0.41 mmol g^{-1}, 0.28 mmol cm^{-3}; fig. S19 and table S5). The improvement in IEC and ion concentration is attributed to the amorphous state of QUPA as confirmed by XRD data (Fig. 2C) (*22*, *35*). Not only does the QUPA/ANF-2.0 have a water content that is 16.6 and 5% higher than QUPA and PVA (table S4) but it also displays a much lower expansion and shrinkage than QUPA and PVA (fig. S20), which is attributed to the interconnected network architecture of this material as represented by GT indices (Table 1). Because of the stiffness and uniformity of the ANF percolated network, the swelling ratio of QUPA/ANF-2.0 is small; it represents only 6.3 and 5.7% in-plane; 9.3 and 7.7% through-plane of that of the QUPA and PVA, respectively (table S5). The lower expansion and shrinkage ratio eliminates shape change during the water gain and loss process and guarantees tight interfacial contact between the electrode and electrolyte essential for zinc-air batteries. This is different from the high IEC designs (*36*, *37*), where high ionic conductivity was gained at the expense of dimensional stability, which is attributed to the cartilage-like design of the ion conductor based on percolating network of nanofibers.

Encouraged by the unique combination of mechanical and ion transport properties of QUPA/ANF-2.0, we evaluated its charge storage performance as a rechargeable zinc-air battery (fig. S21), with the anticipation of using it as protective conformal covers of classical "hard" and leading-edge "soft" robots. It is informative to compare the galvanostatic discharge performance of zinc-air batteries with different electrolytes, namely, PVA, QUPA, and QUPA/ANF-2.0. The discharge plateau of QUPA/ANF-2.0 decreases by only 0.17 V, from 1.27 V at 1.0 mA cm^{-2} to 1.10 V at 5.0 mA cm^{-2}, which is superior to those of PVA and QUPA (Fig. 3B). As shown in Fig. 3C, the maximum discharge capacity of QUPA reached 506.5 mAh g$^{-1}_{Zn}$, whereas that of PVA was only 358.9 mAh g$^{-1}_{Zn}$. An increase of capacity of 624.3 mAh g$^{-1}_{Zn}$ observed for QUPA/ANF-2.0 compared with QUPA confirms the accelerated hydroxide transport. Although both PVA and QUPA/ANF-based batteries have high open-circuit voltage of ≈1.35 V, the cell with QUPA/ANF-2.0 displayed smaller charge-discharge gap and higher power density (Fig. 3, D and E). The maximum power density of 120.3 mW cm^{-2} is much higher than that of QUPA (90.1 mW cm^{-2}) and PVA-based cells (68.5 mW cm^{-2}) and comparable with the best solid or gel-based, flexible zinc-air batteries known (table S6), whereas the charge voltage is lower and the discharge voltage is higher (Fig. 3, F to H). The QUPA/ANF-2.0 zinc-air battery displays negligible potential loss stability and voltage stability improved by almost 100%, even after 108 hours (325 cycles) of charge-discharge polarizations, compared with QUPA (66 hours, 198 cycles) and prototypical PVA (42 hours, 126 cycles) electrolytes that show decreased performance over multiple charge-discharge cycles.

Multiple materials characteristics of the QUPA/ANF-2.0 percolating network composite are responsible for the promising electrochemistry performance of the zinc-air rechargeable batteries. In addition to decreased delamination, QUPA/ANF-2.0 also effectively suppresses dendrite growth. We compared SEM images of the zinc electrodes with different separator-based batteries before and after cycling. On the basis of multiple previous studies (*38*, *39*), the dendrites have a geometry of sharp spikes and plates with high aspect ratio. The metal deposits with this morphology are not observed in Fig. 4 (G and H) but can be distinctly seen in others (Fig. 4, A to F). Besides metallic zinc, chemical phases of zinc oxide and zinc hydroxide that tend to form sharp needles and plates (*12*, *40*–*42*) were observed on the electrodes cycled with PVA and QUPA as seen by SEM (Fig. 4, A to C and D to F) and XRD (fig. S22). On the contrary, well-formed crystalline phase of metallic zinc without high aspect protrusions was observed when zinc electrode was cycled with QUPA/ANF-2.0 (Fig. 4, G to I).

The assembled battery is deformation tolerant (Fig. 5, A and B, and fig. S23, A to D, and movie S1), which enables a biomorphic design of the body-integrated energy storage cells. A zinc-air battery with QUPA/ANF-2.0 electrolyte was tested under various bending conditions with angles ranging from 0° to 180°. At any given shape and bending angle, the charge-discharge cycling curves of the

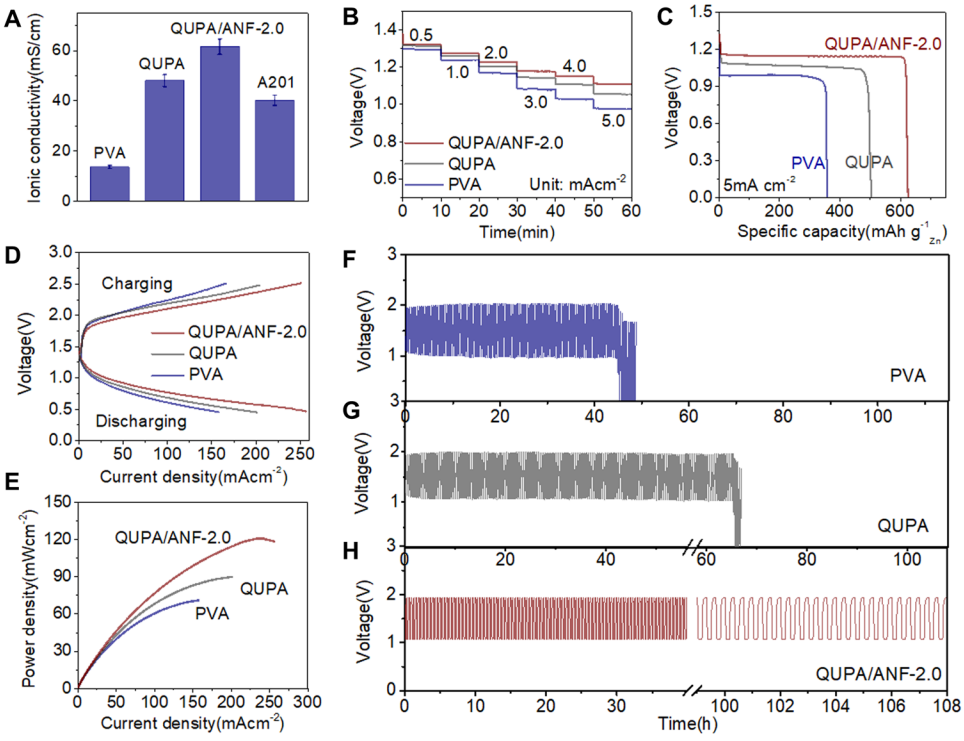

Fig. 3. Electrochemical performance of QUPA/ANF-2.0 and related membranes. (**A**) Comparison of ionic conductivity of the PVA, QUPA, and QUPA/ANF-2.0 membranes; the ion conductivity of a commercial A201 membrane [data taken from (*31*, *33*)]. (**B**) Discharge curve comparison with different electrolytes at various current densities of from 0.5 to 5 mA cm^{-2}. (**C**) Galvanostatic discharge performance of batteries using different membranes at a current density of 5 mA cm^{-2} under atmospheric conditions. (**D** and **E**) Comparison of charge-discharge polarization (D) and power density (E) curves of the batteries with PVA, QUPA, and QUPA/ANF-2.0 electrolytes at room temperature. (**F** to **H**) Galvanostatic charge-discharge cycling comparison of the PVA, QUPA, and QUPA/ANF-2.0 electrolytes at a current density of 1 mA cm^{-2} with a 20 min per cycle period at room temperature.

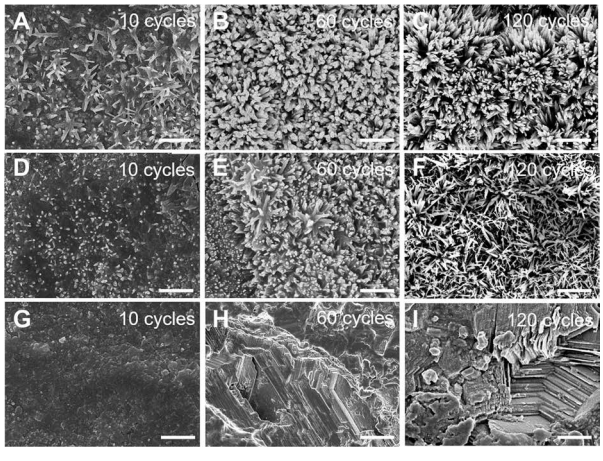

Fig. 4. SEM images of the surface of cycled zinc electrode based on PVA (**A** to **C**) electrolyte, QUPA (**D** to **F**) elecrolyte, and QUPA/ANF-2.0 (**G** to **I**) electrolyte after different number of charge-discharge cycles: (A, D, and G) 10 cycles, (B, E, and H) 60 cycles, and (C, F, and I) 120 cycles. To facilitate the characterization, the zinc electrode surface was thoroughly washed with DI water to remove any electrolytes or salt residues. The needle-like zinc deposits that uniformly form are observed on the electrode surface in the cases of (A) to (F). Scale bars, 2 μm.

battery remained virtually unchanged and showed no significant polarizations, even after 70 hours of cycling (Fig. 5C). The stability of the voltage, charge-discharge polarization curves, power density, and ion-conducting properties at different bend angles (Fig. 5, D and E, and fig. S23, E to G) also confirmed that stable ion transport and power output were not restricted under stressed conditions because of the robust and flexible electrolyte membrane. The total capacity of the structural biomorphic batteries replacing the protective covers of a model robot will be 170 to 340 times higher than that of the current stand-alone Li-ion battery (fig. S24). Compared with a Li-ion battery with the same volume, our biomorphic batteries provide 72 times greater capacity and longer operating time (figs. S25 and S26).

Considering rapid development of soft and flexible robotics and fundamental problems related to implementation of microscale power systems (*43*), it is important to demonstrate their further miniaturization. Taking advantage of the mechanical properties of the QUPA-ANF composites, we integrated them in the body of miniaturized biomorphic robots (minibots) with soft and flexible elements. Despite the mechanical challenges related to the strong deformations and vibrations typical for these devices, several types of minibots were demonstrated: caterpillar, scorpion, spider, and ant (Fig. 6). Successful operation without the stand-alone batteries was also realized (movie S2). The weight of structural batteries in the minibots was only 20% compared with original Li-ion batteries. While increasing the operation time similarly to the hard robots (Fig. 5), the lightness and small volume of our batteries were essential in realization of miniaturization devices.

DISCUSSION

Structural batteries may become an essential part of future robotic technologies because they eliminate the design limitations related to stand-alone batteries. Their successful realization, however, requires the development of a new class of structural power devices with high energy density and deformation tolerance to acquire biomorphic shapes. Ion conductors with biomimetic nanoscale architectures provide the path to realization of biomorphic batteries by providing materials with required combinations of high mechanical, ion transport, and solvation-expansion characteristics. Compared with the prior realization of batteries based on electrolytes with biomimetic nanoscale architecture (*6*, *7*, *44*, *45*), these findings represent conceptual advances both in battery technologies (table S8) and in robotics because they eliminate design constraints related to bulky and heavy charge storage solutions used today. Our structural

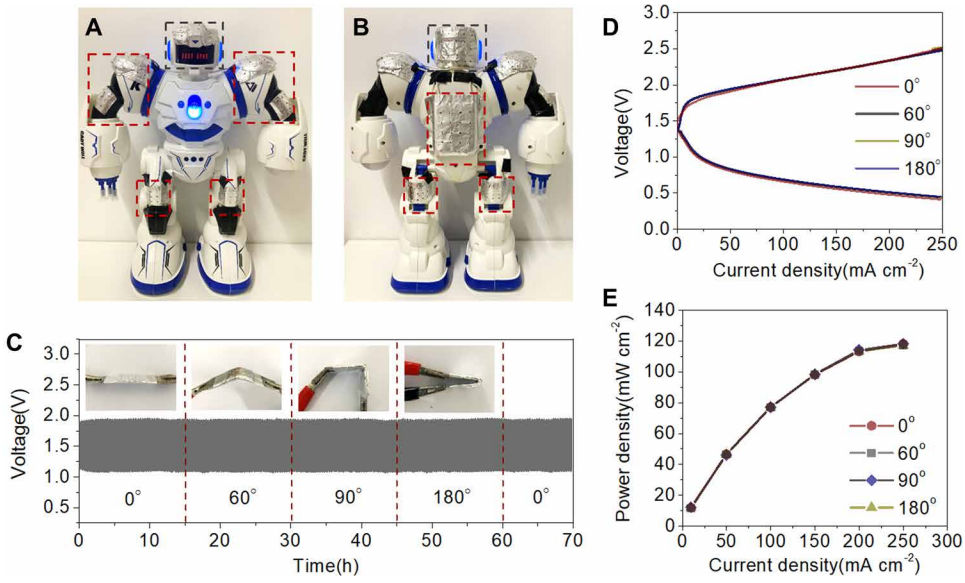

Fig. 5. (**A** and **B**) Photograph of the robot with biomorphic zinc-air battery with different shapes. (**C**) Galvanostatic charge-discharge cycling curves of zinc-air battery with QUPA/ANF-2.0 at a current density of 1 mA cm^{-2} and corresponding photographs, demonstrating the behavior under different bending conditions. (**D**) Comparison of charge-discharge polarization curves of QUPA/ANF-based zinc-air battery under different bending angles. (**E**) The power density comparison of the zinc-air battery at a corresponding current density under different bending angles.

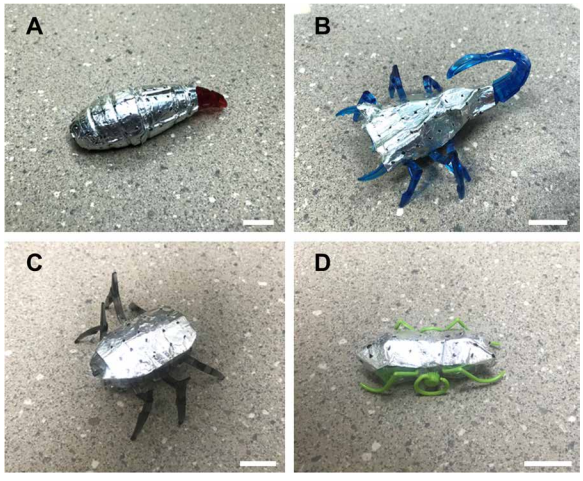

Fig. 6. Structural biomorphic batteries integrated into 'battery-less' miniaturized biomorphic robots (minibots). (**A**) Caterpillar, (**B**) scorpion, (**C**) spider, and (**D**) ant. See Supplementary videos for details on battery removal and robot operation. Scale bar, 2.0 cm.

batteries, based on QUPA/ANF composites with cartilage-like nanofibrous architecture, enabled operational times of more than an order of magnitude compared with a traditional robot with a stand-alone battery. The unique properties of the ion conductors are attributed to the percolating network architecture of ANFs and large contribution of interfaces (*29*) typical for nanofiber composites with polyelectrolytes. GT descriptions of the ANF-based materials open the path to adequate enumeration of their biomimetic organization and further optimization of their performance for specific robotic implementations (movie S3).

MATERIALS AND METHODS

Preparation of ANF networks and their composites

The ANF dispersions were prepared according to a previously reported method (*27*). In brief, 5 g of Kevlar 69 fibers (DuPont Co.) were dissolved in 245 g of DMSO (≥99.7%; Sigma-Aldrich) with 7.5 g of potassium hydroxide (KOH) (Sigma-Aldrich) to obtain 2 wt % ANF dispersions. The dispersions were then magnetically stirred for approximately 1 month at room temperature until they turned viscous and dark red as shown in fig. S6B.

The spin-coating method was then used to prepare the ANF membrane. First, glass slides were precleaned using piranha solution for 2 hours, followed by extensive rinsing with deionized (DI) water (18 megohm) and compressed air drying. Subsequently, about 2 ml of ANF (2 wt %) dispersion was dripped onto the glass slides and spin-coated at 1500 rpm for 30 s (200 rpm for 0.5 wt % ANF dispersion, 500 rpm for 1.0 wt % ANF dispersion, and 1000 rpm for 1.5 wt % ANF dispersion). The prepared membranes were then rinsed with DI water three times to remove the DMSO.

The obtained membranes were stored in DI water for later use. The dried, porous ANF membranes were obtained by complete drying using supercritical CO_2.

Preparation of QUPA and hydroxide ion-conductive QUPA/ANF membranes

Dimethyloctadecyl [3-(trimethoxysilyl)propyl]ammonium chloride (DMOAP) (42 wt % in methanol; Sigma-Aldrich) was used as the precursor for functionalizing the polymer. First, 5 g of PVA (molecular weight = 178,000, 99 + %; Sigma-Aldrich) was dissolved and stirred in 95 ml of DI water at 90°C to get a 5 wt % uniform solution. DMOAP was then added into the above solution in the mass ratio of DMOAP:PVA being 10:1. The reaction was carried out at room temperature under magnetic stirring for 24 hours. DMOAP functionalizes PVA (fig. S2), adding positively charged quaternary ammonium groups to facilitate the ion transport of negatively charged hydroxide ions (*46*). The modification process was confirmed by Fourier transform infrared (FTIR), x-ray photoelectron spectroscopy (XPS), and SEM images (Fig 2, A and B, and figs. S3 to S5).

The hydroxide-conductive QUPA/ANF membranes were prepared through immersion, cross-linking, and ion-exchange processes (fig. S2). First, the obtained ANF membrane was immersed into the above polymer solution for 2 days (fig. S1), making sure that the polymer solution was fully filled into the ANF framework. Then, the extra polymer solution on the membrane's surface was removed [Method: The QUPA/ANF composite membrane was taken out of the QUPA polymer solution and clamped between two polytetrafluoroethylene (PTFE) sheets. Applying an external force between the two PTFE sheets, the extra polymer on the surface of the membrane was extruded and removed.]. QUPA-ANF membranes were subsequently

dried at room temperature for 12 hours and then cross-linked at 60°C under vacuum for another 24 hours. The cross-linked composite membrane was then immersed in 1 M KOH solution to process the ion exchange and equilibrated for 12 hours to convert the chloride (Cl^-) counter ions into hydroxide ions (OH^-). The hydroxide-conductive membranes were placed in a freezer at −20°C for 3 hours, followed by thawing at room temperature. The corresponding functionalization process is shown in fig. S2. The preparation of the QUPA membrane is similar to the above process except for the addition of ANF. For comparison, the PVA/KOH gel electrolyte was prepared according to a previously published work (*7*).

Fabrication of rechargeable zinc-air batteries

A rechargeable zinc-air battery was fabricated using a stack assembly method, where the electrodes were placed face-to-face with the QUPA/ANF-2.0 membrane. Zinc foil (0.5 mm; Sigma-Aldrich) was used as the anode electrode. An air electrode was prepared by Pt/C (Sigma-Aldrich) and IrO_2 (99.9%; Sigma-Aldrich) as the bifunctional electroactive material and then sprayed onto a carbon cloth (Fisher Scientific). A dispersion of the catalyst consisting of 5 mg of Pt/C, 5 mg of IrO_2, 67 μl of 5 wt % Nafion (LIQUion solution, Ion Power Inc.), and 1.0 ml of 1-propanol (Sigma-Aldrich) was sprayed onto a carbon cloth (2.5 cm by 3.0 cm) (Fuel Cell Technology) as the gas diffusion layer with a catalyst loading of 1.0 mg cm^{-2}. After spraying, the electrode was dried in an oven at 60°C for 1 hour (*16*).

Structural characterization and electrochemical measurements

SEM (FEI Nova Nanolab dual-beam FIB) and transmission electron microscopy (TEM) (JEOL 3011 HRTEM) were used to image the morphologies of the PVA, QUPA, ANF, and QUPA/ANF-based membranes. FTIR spectra (Nicolet 6700 spectrometer), XPS (PerkinElmer PHI 1600 ESCA), and XRD (Rigaku Rotating Anode XRD with Cu Kα radiation generated at 40 kV and 100 mA) were used to analyze the chemistry composition and structure of the ANF membrane and functionalized QUPA and QUPA/ANF membranes. The mechanical properties of ANF, QUPA, and QUPA/ANF membranes were investigated using a TA XT Plus Texture Analyzer (Stable Micro Systems Ltd.). The membrane was cut into rectangular strips (20 mm by 5 mm), and 20 samples were tested in each trial under a strain rate of 2.0 mm min^{-1} at about 22°C and 20 to 30% humidity. The tensile toughness (U) was calculated by integrating the area under tensile curves, as expressed by the following equation

$$U = \sum_{i=0}^{n} \sigma\varepsilon_i$$

where σ and ε refer to the tensile stress and strain at failure, respectively.

The Quantachrome AUTOSORB 6B system was used to characterize the pore width of the dried porous ANF membrane and QUPA/ANF composite membrane using nitrogen sorption at 77.4 K. The porous ANF membrane was obtained by complete drying using supercritical CO_2; the drying method maintained the membrane's pore size. In addition, the pore size distribution of the ANF membrane was calculated by Barrett-Joyner-Halenda methods. The thermal stability was analyzed by TA Instruments Discovery thermogravimetric analyzer with a temperature ramp to 800°C at 10°C min^{-1} in Ar atmosphere at a flow rate of 30 ml min^{-1}.

Electrochemical impedance spectroscopy (Autolab Potentiostat and Solartron 1260 frequency response analyzer) was carried out in the frequency range from 100 kHz to 0.05 Hz with a potential amplitude of 20 mV. The battery charge and discharge polarization data were collected using the galvanodynamic method at a scan rate of 1.0 mA s^{-1} with a cutoff voltage of 0.45 V for the discharge and 2.5 V for the charge. Discharge capacity performance was tested at a current density of 5.0 mA cm^{-2}, and the capacity was calculated by the consumed zinc mass. Discharge and charge cycling performances were carried out by a recurrent galvanic pulse method at a fixed current density of 1 mA cm^{-2}, with each cycle consisting of 10 min for discharge followed by 10 min for charge.

Integration of biomorphic batteries in robots

Structural biomorphic batteries were made from stacked zinc foil/QUPA/ANF-2.0/carbon cloth with Pt/C and IrO_2 cells. The outer protective layer of battery was flexible and porous Al foil and connected with insulating glue to prevent short circuit. When needed, three cells were then connected in series and attached on the surface in robots providing ~4.0 V output potential. The biomorphic shapes of the batteries were adapted to serve as protective covers to scaled-up hard robots and miniaturized robotic devices with soft elements. In all of them, these biomorphic, structural batteries replaced the main power source.

Graph theoretical analysis of the percolating network architecture of ANF-based materials

The protocol for the GT processing of microscopy images by StructuralGT initially involved image processing by the scikit-image Python library. First, a median filter was applied to reduce noise, and then a binary image was created by selecting the top 50% of pixels with the highest intensity to distinguish individual filaments in the foreground from the fibers in the background. The black-and-white binary image was subsequently converted into a skeleton image serving as a graph prototype. The ANF filaments in these images were represented by a string of single pixels. After removing dead-end edges and isolated fragments not connected to the main network, the clusters of nodes within a defined radius of the central node were consolidated into a single node through the use of the mahotas Python module by identifying branching points on the skeleton and applying a small mask element over them. The final conversion of the corrected skeleton into a graph dictionary object was carried out with the sknw Python module. Generated graphs were plotted on top of the corresponding binary images using the package MatPlotLib, where the determined nodes are represented by red dots, and the edges are represented by green lines in the GT representations in Fig. 1. The NetworkX Python module was used to read out the graph dictionary and perform the calculations of GT indices.

Multifractal analysis

MFA is a mathematical tool used to quantify the structural complexity and heterogeneity of complex networks (i.e., the multifractality of a graph provides information about the higher-order statistics and goes beyond clustering metrics). The multifractal features of a graph structure can be quantified via a finite box-covering method (*18*). The graph is considered to be fractal if the relationship of l (the size of the box) and $N(l)$ (the number of boxes of size l covering the graph nodes) satisfies $N(l) \sim l^{\alpha}$, where α is the Lipschitz-Holder exponent representing the fractal dimension of a certain fractal structure. Furthermore, the network is considered to be multifractal

if the relationship of l (the size of the box) and $B(\alpha)$ (the number of boxes with exponent α) satisfies $B(\alpha) \sim l^{-f(\alpha)}$, where $f(\alpha)$ is the singularity or multifractal spectrum. To study the different fractal structures in the multifractal network, the distorting exponent, q, and mass exponent, $\tau(q)$, are used for distinguishing the details of different fractal structures. The box-counting method uses the same size boxes to cover the entire graph, and then the relationship of l (the size of each box) and $N_i(l)$ (the number of nodes in the i_{th} box of size l) should satisfy $\sum_i N_i(l)^q \sim l^{\tau(q)}$. The relationship between the pair of $(\tau(q),q)$ and $(f(\alpha),\alpha)$ is obtained by the Legendre transformation as (*48*)

$$\alpha = \frac{d\tau(q)}{dq}$$

$$f(\alpha) = q\alpha - \tau(q)$$

In this way, the multifractal spectrum characterizes all the heterogeneous fractal topological structures of a graph and provides information about the number of topological rules and their variation that govern the network organization.

SUPPLEMENTARY MATERIALS

robotics.sciencemag.org/cgi/content/full/5/45/eaba1912/DC1
Materials and Methods
Fig. S1. Schematic diagram of overall preparation of the QUPA/ANF membranes.
Fig. S2. Proposed reaction mechanism for PVA chains functionalization with DMOAP.
Fig. S3. PVA and functionalized QUPA composite comparison by XPS spectrum.
Fig. S4. Top-view SEM images of the PVA and QUPA membranes at different magnifications.
Fig. S5. SEM and corresponding EDS mapping images of PVA and QUPA membranes.
Fig. S6. Preparation of ANFs.
Fig. S7. Thermogravimetry curve comparison for the QUPA/ANF composite membrane with different ANF dispersion concentrations.
Fig. S8. SEM images of cross-section morphology of ANF and QUPA/ANF membranes.
Fig. S9. The morphology and color comparisons of the ANF-2.0 membrane after immersing into QUPA polymer solution.
Fig. S10. The pore surface area comparison of porous ANF-2.0 membrane and QUPA/ANF-2.0 composite membrane according to the BET analysis.
Fig. S11. The toughness values of QUPA/ANF with different ANF dispersion concentrations from 0.5 to 2.0 wt %.
Fig. S12. The initial impedance spectra comparison of QUPA/ANF composite membrane with different ANF dispersion concentrations.
Fig. S13. Digital photos of the folding and releasing process of QUPA/ANF-2.0 membrane.
Fig. S14. SEM images of QUPA/ANF-2.0 membrane under different states.
Fig. S15. Fracture energy of QUPA/ANF-2.0 membrane.
Fig. S16. The initial impedance spectra comparison of PVA, QUPA, and QUPA/ANF-2.0.
Fig. S17. The temperature-dependent ionic conductivity comparison of PVA, QUPA, and QUPA/ANF-2.0 membranes.
Fig. S18. The Arrhenius plot comparison of PVA, QUPA, and QUPA/ANF-2.0 membranes.
Fig. S19. The ion concentration and IEC comparison of PVA, QUPA, and QUPA/ANF-2.0 membranes.
Fig. S20. Comparison of the shape changes of QUPA and QUPA/ANF-2.0 membranes after drying at room temperature until a constant weight and dimension were obtained.
Fig. S21. Schematic representation of the rechargeable zinc-air battery.
Fig. S22. The XRD pattern of the cycled zinc electrode with QUPA electrolyte.
Fig. S23. The performance of zinc-air battery with different bending angles.
Fig. S24. Robot measures used in the calculations of its surface area.
Fig. S25. The size of original Li-ion battery.
Fig. S26. Comparison of working time of the robot with original Li-ion battery and six structural zinc-air batteries.
Table S1. Graph theoretical enumerators for description of ANF percolating network materials characterizing network connectivity.
Table S2. Comparison of tensile strength, tensile modulus, and elongation at break of QUPA, ANF, and QUPA/ANF composite membranes.
Table S3. Comparison of tensile strength, Young's modulus, and elongation at break data for different fiber enhanced polymer hydrogels.
Table S4. Comparison of ionic conductivities of previously developed solid or gel electrolytes.
Table S5. Comparison of ionic conductivity, IEC, ion concentration, water uptake, and swelling ratio of QUPA and QUPA/ANF composite membranes.
Table S6. Summary of solid or gel state flexible rechargeable zinc-air batteries with various electrocatalysts and electrolytes.
Table S7. Summary of the surface area of the robot with different parts of robot.
Table S8. Comparison of battery properties from this work and in drones in (*6*).
Movie S1. The demonstration of biomorphic structural battery in battery-less humanoid robotic device.
Movie S2. The demonstration of biomorphic structural battery in battery-less scorpion minibot.
Movie S3. Overview of design and implementation of biomimetic composites and biomorphic structural batteries for robotics.

REFERENCES AND NOTES

1. M. Coelho, T. Oliveira, R. Fernandes, Biochemistry of adipose tissue: An endocrine organ. *Arch. Med. Sci.* **9**, 191–200 (2013).
2. L. M. Schneider, N. Ihrner, D. Zenkert, M. Johansson, Bicontinuous electrolytes via thermally initiated polymerization for structural lithium ion batteries. *ACS Appl. Energy Mater.* **2**, 4362–4369 (2019).
3. C. González, J. J. Vilatela, J. M. Molina-Aldareguía, C. S. Lopes, J. LLorca, Structural composites for multifunctional applications: Current challenges and future trends. *Prog. Mater. Sci.* **89**, 194–251 (2017).
4. W. Johannisson, N. Ihrner, D. Zenkert, M. Johansson, D. Carlstedt, L. E. Asp, F. Sieland, Multifunctional performance of a carbon fiber UD lamina electrode for structural batteries. *Compos. Sci. Technol.* **168**, 81–87 (2018).
5. Y. Zhang, J. Ma, A. K. Singh, L. Cao, J. Seo, C. D. Rahn, C. E. Bakis, M. A. Hickner, Multifunctional structural lithium-ion battery for electric vehicles. *J. Intell. Mater. Syst. Struct.* **28**, 1603–1613 (2017).
6. M. Wang, A. Emre, S. O. Tung, A. Gerber, D. Wang, Y. Huang, V. Cecen, N. A. Kotov, Biomimetic solid-state Zn^{2+} electrolyte for corrugated structural batteries. *ACS Nano* **13**, 1107–1115 (2019).
7. J. Fu, Z. P. Cano, M. G. Park, A. Yu, M. Fowler, Z. Chen, Electrically rechargeable zinc–air batteries: Progress, challenges, and perspectives. *Adv. Mater.* **29**, 1604685 (2017).
8. Y. Li, H. Dai, Recent advances in zinc–air batteries. *Chem. Soc. Rev.* **43**, 5257–5275 (2014).
9. X. Han, X. Wu, C. Zhong, Y. Deng, N. Zhao, W. Hu, $NiCo_2S_4$ nanocrystals anchored on nitrogen-doped carbon nanotubes as a highly efficient bifunctional electrocatalyst for rechargeable zinc–air batteries. *Nano Energy* **31**, 541–550 (2017).
10. A. R. Mainar, O. Leonet, M. Bengoechea, I. Boyano, I. de Meatza, A. Kvasha, A. Guerfi, J. A. Blázquez, Alkaline aqueous electrolytes for secondary zinc–air batteries: An overview. *Int. J. Energy Res.* **40**, 1032–1049 (2016).
11. D. U. Lee, J. Scott, H. W. Park, S. Abureden, J.-Y. Choi, Z. Chen, Morphologically controlled Co_3O_4 nanodisks as practical bi-functional catalyst for rechargeable zinc–air battery applications. *Electrochem. Commun.* **43**, 109–112 (2014).
12. J. F. Parker, C. N. Chervin, E. S. Nelson, D. R. Rolison, J. W. Long, Wiring zinc in three dimensions re-writes battery performance–dendrite-free cycling. *Energ. Environ. Sci.* **7**, 1117–1124 (2014).
13. M. Yang, K. Cao, L. Sui, Y. Qi, J. Zhu, A. Waas, E. M. Arruda, J. Kieffer, M. D. Thouless, N. A. Kotov, Dispersions of aramid nanofibers: A new nanoscale building block. *ACS Nano* **5**, 6945–6954 (2011).
14. S.-O. Tung, S. Ho, M. Yang, R. Zhang, N. A. Kotov, A dendrite-suppressing composite ion conductor from aramid nanofibres. *Nat. Commun.* **6**, 6152 (2015).
15. X. Yao, Y. Hu, B. Cao, R. Peng, J. Ding, Effects of surface molecular chirality on adhesion and differentiation of stem cells. *Biomaterials* **34**, 9001–9009 (2013).
16. L. Wang, Y. Yu, P. C. Chen, D. W. Zhang, C. H. Chen, Electrospinning synthesis of C/Fe_3O_4 composite nanofibers and their application for high performance lithium-ion batteries. *J. Power Sources* **183**, 717–723 (2008).
17. L. Xu, X. Zhao, C. Xu, N. A. Kotov, Water-rich biomimetic composites with abiotic self-organizing nanofiber network. *Adv. Mater.* **30**, 1703343 (2018).
18. Y. Xue, P. Bogdan, Reliable multi-fractal characterization of weighted complex networks: Algorithms and implications. *Sci. Rep.* **7**, 7487 (2017).
19. C.-C. Yang, Chemical composition and XRD analyses for alkaline composite PVA polymer electrolyte. *Mater. Lett.* **58**, 33–38 (2004).
20. B. Wu, L. Ge, D. Yu, L. Hou, Q. Li, Z. Yang, T. Xu, Cationic metal–organic framework porous membranes with high hydroxide conductivity and alkaline resistance for fuel cells. *J. Mater. Chem. A* **4**, 14545–14549 (2016).
21. Z. Gadjourova, Y. G. Andreev, D. P. Tunstall, P. G. Bruce, Ionic conductivity in crystalline polymer electrolytes. *Nat. Commun.* **412**, 520–523 (2001).
22. K. H. Gopi, S. D. Bhat, Anion exchange membrane from polyvinyl alcohol functionalized with quaternary ammonium groups via alkyl spacers. *Ionics* **24**, 1097–1109 (2018).
23. M. Yang, K. Cao, B. Yeom, M. D. Thouless, A. Waas, E. M. Arruda, N. A. Kotov, Aramid nanofiber-reinforced transparent nanocomposites. *J. Compos. Mater.* **49**, 1873–1879 (2015).

24. Y. Guan, W. Li, Y. Zhang, Z. Shi, J. Tan, F. Wang, Y. Wang, Aramid nanofibers and poly (vinyl alcohol) nanocomposites for ideal combination of strength and toughness via hydrogen bonding interactions. *Compos. Sci. Technol.* **144**, 193–201 (2017).
25. H. Zarrin, S. Sy, J. Fu, G. Jiang, K. Kang, Y.-S. Jun, A. Yu, M. Fowler, Z. Chen, Molecular functionalization of graphene oxide for next-generation wearable electronics. *ACS Appl. Mater. Interface* **8**, 25428–25437 (2016).
26. M. Wang, N. Xu, J. Fu, Y. Liu, J. Qiao, High-performance binary cross-linked alkaline anion polymer electrolyte membranes for all-solid-state supercapacitors and flexible rechargeable zinc–air batteries. *J. Mater. Chem. A* , 11257–11264 (2019).
27. I. Villaluenga, K. H. Wujcik, W. Tong, D. Devaux, D. H. C. Wong, J. M. DeSimone, N. P. Balsara, Compliant glass–polymer hybrid single ion-conducting electrolytes for lithium batteries. *Proc. Natl. Acad. Sci. U.S.A.* **113**, 52–57 (2016).
28. N. Kamaya, K. Homma, Y. Yamakawa, M. Hirayama, R. Kanno, M. Yonemura, T. Kamiyama, Y. Kato, S. Hama, K. Kawamoto, A. Mitsui, A lithium superionic conductor. *Nat. Mater.* **10**, 682–686 (2011).
29. B. Yeom, T. Sain, T. Lacevic, D. Bukharina, S.-H. Cha, A. M. Waas, E. M. Arruda, N. A. Kotov, Abiotic tooth enamel. *Nature* **543**, 95–98 (2017).
30. N. A. Kotov, I. Dékány, J. H. Fendler, Ultrathin graphite oxide–polyelectrolyte composites prepared by self-assembly: Transition between conductive and non-conductive states. *Adv. Mater.* **8**, 637–641 (1996).
31. C. Lin, S. S. Shinde, X. Li, D.-H. Kim, N. Li, Y. Sun, X. Song, H. Zhang, C. H. Lee, S. U. Lee, J.-H. Lee, Solid-state rechargeable zinc–air battery with long shelf life based on nanoengineered polymer electrolyte. *ChemSusChem* **11**, 3215–3224 (2018).
32. Y. Wei, M. Wang, N. Xu, L. Peng, J. Mao, Q. Gong, J. Qiao, Alkaline exchange polymer membrane electrolyte for high performance of all-solid-state electrochemical devices. *ACS Appl. Mater. Interfaces* **10**, 29593–29598 (2018).
33. J. Fu, J. Zhang, X. Song, H. Zarrin, X. Tian, J. Qiao, L. Rasen, K. Li, Z. Chen, A flexible solid-state electrolyte for wide-scale integration of rechargeable zinc–air batteries. *Energ. Environ. Sci.* **9**, 663–670 (2016).
34. J. Zhang, J. Fu, X. Song, G. Jiang, H. Zarrin, P. Xu, K. Li, A. Yu, Z. Chen, Laminated cross-linked nanocellulose/graphene oxide electrolyte for flexible rechargeable zinc–air batteries. *Adv. Energy Mater.* **6**, 1600476 (2016).
35. X. Wu, W. Chen, X. Yan, G. He, J. Wang, Y. Zhang, X. Zhu, Enhancement of hydroxide conductivity by the di-quaternization strategy for poly(ether ether ketone) based anion exchange membranes. *J. Mater. Chem. A* **2**, 12222–12231 (2014).
36. N. J. Robertson, H. A. Kostalik IV, T. J. Clark, P. F. Mutolo, H. D. Abruña, G. W. Coates, Tunable high performance cross-linked alkaline anion exchange membranes for fuel cell applications. *J. Am. Chem. Soc.* **132**, 3400–3404 (2010).
37. M. Tanaka, K. Fukasawa, E. Nishino, S. Yamaguchi, K. Yamada, H. Tanaka, B. Bae, K. Miyatake, M. Watanabe, Anion conductive block poly(arylene ether)s: Synthesis, properties, and application in alkaline fuel cells. *J. Am. Chem. Soc.* **133**, 10646–10654 (2011).
38. K. J. Harry, D. T. Hallinan, D. Y. Parkinson, A. A. MacDowell, N. P. Balsara, Detection of subsurface structures underneath dendrites formed on cycled lithium metal electrodes. *Nat. Mater.* **13**, 69–73 (2014).
39. M. J. Zachman, Z. Tu, S. Choudhury, L. A. Archer, L. F. Kourkoutis, Cryo-STEM mapping of solid–liquid interfaces and dendrites in lithium-metal batteries. *Nature* **560**, 345–349 (2018).
40. K. Wang, P. Pei, Z. Ma, H. Chen, H. Xu, D. Chen, X. Wang, Dendrite growth in the recharging process of zinc–air batteries. *J. Mater. Chem. A* **3**, 22648–22655 (2015).
41. K. E. K. Sun, T. K. A. Hoang, T. N. L. Doan, Y. Yu, X. Zhu, Y. Tian, P. Chen, Suppression of dendrite formation and corrosion on zinc anode of secondary aqueous batteries. *ACS Appl. Mater. Interfaces* **9**, 9681–9687 (2017).
42. G. Garcia, E. Ventosa, W. Schuhmann, Complete prevention of dendrite formation in Zn metal anodes by means of pulsed charging protocols. *ACS Appl. Mater. Interfaces* **9**, 18691–18698 (2017).
43. C. Lu, V. Raghunathan, K. Roy, Micro-scale energy harvesting: A system design perspective, in *15th Proceedings of the Asia and South Pacific Design Automation Conference, ASP-DAC* (IEEE, 2010), pp. 89–94.
44. A. Malti, J. Edberg, H. Granberg, Z. U. Khan, J. W. Andreasen, X. Liu, D. Zhao, H. Zhang, Y. Yao, J. W. Brill, I. Engquist, M. Fahlman, L. Wågberg, X. Crispin, M. Berggren, An organic mixed ion–electron conductor for power electronics. *Adv. Sci.* **3**, 1500305 (2016).
45. L. Hu, N. Liu, M. Eskilsson, G. Zheng, J. McDonough, L. Wågberg, Y. Cui, Silicon-conductive nanopaper for Li-ion batteries. *Nano Energy* **2**, 138–145 (2013).
46. R. Ludwig, New insight into the transport mechanism of hydrated hydroxide ions in water. *Angew. Chemie Int. Ed.* **42**, 258–260 (2003).
47. X. Chen, B. Liu, C. Zhong, Z. Liu, J. Liu, L. Ma, Y. Deng, X. Han, T. Wu, W. Hu, J. Lu, Ultrathin Co_3O_4 layers with large contact area on carbon fibers as high-performance electrode for flexible zinc–air battery integrated with flexible display. *Adv. Energy Mater.* **7**, 1700779 (2017).
48. B. B. Mandelbrot, *Multifractals and 1/f Noise: Wild Self-Affinity in Physics (1963–1976)* (Springer Mathematics, 2013).

Funding: N.A.K. acknowledges the support from Vannewar Bush DoD Fellowship titled "Engineered chiral ceramics" (ONR N000141812876) "Energy- and cost-efficient manufacturing employing nanoparticles" (NSF 1463474), and "Layered composites from branched nanofibers for lithium ion batteries" (NSF 1538180), and "Nanocomposite ion conductors for thin film batteries" (AFOSR FA9550-16-1-0265). M.W. acknowledges the support from the China Scholarship Council, Postdoctoral fellow of Harbin Institute of Technology. P.B. acknowledges the support from the National Science Foundation (NSF) Career Award CPS/CNS-1453860 and the DARPA Young Faculty Award and DARPA Director Award, under grant number N66001-17-1-4044. **Author contributions:** M.W. prepared QUPA-ANF composites, performed characterization experiments, and cowrote the paper. A.E., C.W., and Z.J. prepared and characterized ANF composites and analyzed batteries performance. D.V. wrote the Python script for StructuralGT and carried out GT calculations of major indexes. X.X. and P.B. calculated the multifractal description of nanofiber composites. Y.H. analyzed the results and participated in writing the paper. N.A.K. conceptualized the study, GT design of composites, calculated GT indexes, and cowrote the paper. **Competing interests:** N.A.K. is a founder of Elegus Technologies that produces ANF-based separators. N.A.K., A.E., and M.W. are inventors on patent application (insert number) held/submitted by The University of Michigan that covers structural zinc batteries. **Data and materials availability:** All data needed to evaluate the conclusions in the paper are present in the paper or the Supplementary Materials.

Submitted 12 November 2019
Accepted 23 July 2020
Published 19 August 2020
10.1126/scirobotics.aba1912

Citation: M. Wang, D. Vecchio, C. Wang, A. Emre, X. Xiao, Z. Jiang, P. Bogdan, Y. Huang, N. A. Kotov, Biomorphic structural batteries for robotics. *Sci. Robot.* **5**, eaba1912 (2020).

Science Robotics

Biomorphic structural batteries for robotics

Mingqiang Wang, Drew Vecchio, Chunyan Wang, Ahmet Emre, Xiongye Xiao, Zaixing Jiang, Paul Bogdan, Yudong Huang, and Nicholas A. Kotov

Sci. Robot. **5** (45), eaba1912. DOI: 10.1126/scirobotics.aba1912

Science Robotics (ISSN 2470-9476) is published by the American Association for the Advancement of Science. 1200 New York Avenue NW, Washington, DC 20005. The title *Science Robotics* is a registered trademark of AAAS.